2004-07-08

Wideband Channel Characterization for MIMO Scenario

Justin T. Holzer
Brigham Young University - Provo

WIDEBAND CHANNEL CHARACTERIZATION FOR MIMO SCENARIO

by

Justin T. Holzer

A thesis submitted to the faculty of

Brigham Young University

in partial fulfillment of the requirements for the degree of

Master of Science

Department of Electrical and Computer Engineering

Brigham Young University

August 2004

BRIGHAM YOUNG UNIVERSITY

GRADUATE COMMITTEE APPROVAL

of a thesis submitted by

Justin T. Holzer

This thesis has been read by each member of the following graduate committee and by majority vote has been found to be satisfactory.

Date	Michael A. Jensen, Chair
Date	Michael D. Rice
Date	Karl F. Warnick

BRIGHAM YOUNG UNIVERSITY

As chair of the candidate's graduate committee, I have read the thesis of Justin T. Holzer in its final form and have found that (1) its format, citations, and bibliographical style are consistent and acceptable and fulfill university and department style requirements; (2) its illustrative materials including figures, tables, and charts are in place; and (3) the final manuscript is satisfactory to the graduate committee and is ready for submission to the university library.

Date

Michael A. Jensen
Chair, Graduate Committee

Accepted for the Department

A. Lee Swindlehurst
Graduate Coordinator

Accepted for the College

Douglas M. Chabries
Dean, College of Engineering and Technology

ABSTRACT

WIDEBAND CHANNEL CHARACTERIZATION FOR MIMO SCENARIO

Justin T. Holzer

Department of Electrical and Computer Engineering

Master of Science

Because broadband wireless systems benefit from accurate channel characterization, there is growing interest in broadband wireless multiple-input multiple-output (MIMO) channel models. This thesis verifies the suitability of the Saleh Valenzuela with Angle (SVA) model for wideband MIMO communication models. While recent wideband MIMO measurements have been obtained by switching a single transmit/receive pair over all possible antenna pair combinations, a simultaneous probing system is superior because of the time required for the antenna-switching channel measurements. This work provides two different wideband channel estimation algorithms based on simultaneous transmission from and reception on all antennas.

Simulated data from an electromagnetic ray tracing tool is used (as a substitute for measured data) to obtain propagation data. One of the wideband estimation algorithms is then used to extract MIMO channel data from propagation data. From these estimated channels, parameters such as capacity, coherence bandwidth, RMS delay spread and maximum delay spread are compared (statistically) to those obtained from the SVA model. The comparisons of the different parameters show the ability of the SVA model to simulate wideband MIMO communication channels.

Contents

List of Tables

List of Figures

Chapter 1

Introduction

1.1 Background

Indoor communication has become an increasingly interesting application for wireless communication systems. For example, wireless technology is an excellent choice for temporary networks, or for systems with mobile subscribers. Even for fixed subscriber locations, the convenience of wireless sometimes makes it the solution of choice. A perfect example of the popularity of the communication approach has been the recent success of wireless local area network (WLAN) equipment.

One difficulty with wireless communication in indoor environments is that the propagating wave carrying the signal scatters from walls, door frames, furniture, etc. As a result, the signal arrives at the receiver via many different paths, a type of propagation referred to as multipath propagation. Figure 1.1 shows one such path resulting from one scatterer in the environment. The combination of these multiple signals at the receiver can lead to strong signal fluctuation that can severely degrade the connection quality.

While the destructive interference created by multipath propagation is typically detrimental to communication throughput, multiple antennas can be used to dramatically improve communication over such channels [1]. If multiple transmit and receive antennas are used, the system is referred to as a multiple input multiple output (MIMO) system. For very rich multipath channels, systems utilizing N_T transmit and N_R receive antennas can communicate over $\mathbf{N} = \min(N_T, N_R)$ independent data

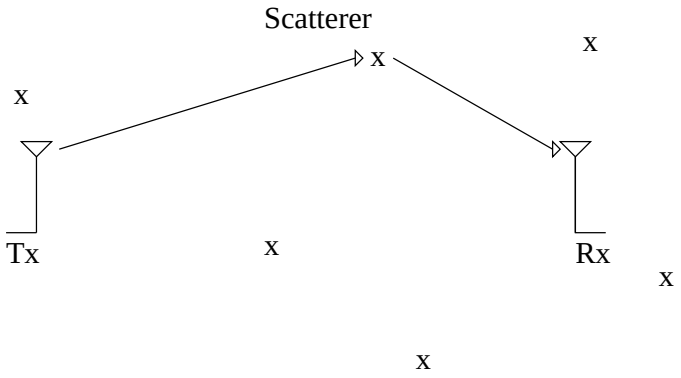

Figure 1.1: Illustration of scatterers in multipath wireless channel

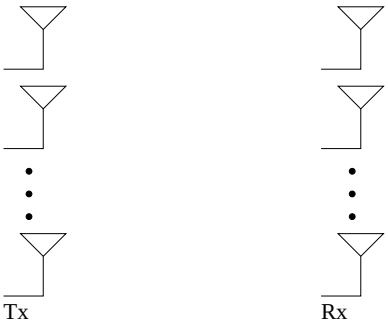

Figure 1.2: MIMO antenna array

streams. The result is increased system throughput without an increase in spectral bandwidth required [2]. Capacity is used to indicate the system throughput.

Accurately simulating the performance of a MIMO systems requires the availability of an accurate statistical model of the MIMO channel. Statistical models for the narrowband multipath channel have been proposed recently by Saleh and Valenzuela [3] and Spencer [4]. Other work by Wallace [2] has demonstrated the accuracy of statistical models for indoor multipath channels. While this prior work has provided invaluable information concerning narrowband channels, there has yet to be a comprehensive study on the modelling of wideband channels where the MIMO transfer matrix varies with frequency. This topic is the focus of this thesis.

1.2 Problem Statement

The goal of this thesis is to explore the suitability of previously developed statistical channel models [3], [4] for characterizing the broadband behavior of MIMO channels. To accomplish this goal, the original research plan called for utilizing a broadband channel probing platform currently under development in the laboratory to directly measure the channel in a typical indoor environment. The statistics of several quantities relating to the time/frequency characteristics of the measured channel would then be compared to the same statistics generated by the channel models. This procedure is very similar to that followed in [5] for narrowband channel characterization.

The difficulty with this plan was that the experimental platform development took much longer than anticipated, and therefore no data was available at the time of this writing. As a result, channel data obtained using a ray tracing simulation tool is used in this thesis as a surrogate for the experimentally collected data. All other information concerning experiment deployment and data processing is provided along with simulations demonstrating the performance of all techniques proposed.

1.3 Summary of Contributions

This thesis builds on some of the more recent work in narrowband MIMO channel characterization to examine wideband MIMO channel characteristics. Several contributions are detailed in the following chapters relating to the overall goal of wideband channel evaluation.

First, the thesis develops two different wideband channel estimation algorithms, referred to as the multi-measurement solution and the single measurement solution. Each of these algorithms were implemented and compared as part of this work. It is noteworthy that these algorithms are based on the premise of simultaneous transmission from and reception on all antennas. This is in contrast to recent measurements obtained by switching a single transmit/receive pair over all possible antenna pair combinations [6], [7], [8]. The simultaneous probing system is superior

since the switched arrangement can require up to five minutes to measure the channel at a single location [9].

The ray tracing tool used to simulate indoor wideband data measurement is presented. The fourth floor of the Clyde Building on the Brigham Young University campus has been constructed within the ray tracing framework and serves as the target environment. Permanent structures are modelled in the ray tracing simulation environment with the transmit and receive arrays placed at any desired location on the floor plan.

The simulated channels from the ray tracing tool are analyzed and compared with the channels generated using the Saleh Valenzuela with Angle (SVA) model. A few parameters of practical interest are presented to describe the channel and its characteristics. For example, the wideband MIMO capacity is analyzed for the ray tracing channels and the SVA channels. The coherence bandwidth, defined as the "maximum frequency difference for which two signals have a specified value of correlation" [10], is also examined for two specific values of correlation. Several time domain parameters are then analyzed by use of the power time-delay profile to compare the results of the wideband channels, including the root mean square (RMS) delay spread, the delay interval and the maximum delay interval.

1.4 Thesis Outline

The thesis proceeds as follows. Chapter 2 provides background material on existing indoor channel multipath models and capacity computation of narrowband MIMO channels. Chapter 3 then details the channel estimation algorithms developed for this work, and uses simulations to compare their relative performance. In Chapter 4, one of these estimators is used to extract MIMO channel data from propagation data obtained from ray tracing simulations. While this channel estimation is an unnecessary step since the data is obtained from simulation, it is applied here in the spirit of using the ray tracing data as a direct substitute of the measured data. This also provides additional verification of the estimation algorithm suitability. Finally, channel parameters derived from these estimated channels are compared (statistically)

to those obtained from the SVA model. Some brief conslusions are then drawn in Chapter 5.

Chapter 2

Background

This chapter gives a short background on the work that has been done in the area of MIMO communications that is relevant to the work in this thesis. It outlines the existing model by Saleh and Valenzuela [3] and an extension to the model by Spencer [4]. A summary of other work on channel modelling, channel capacity and important channel parameters is also provided. The chapter concludes with a brief tutorial on the water-filling solution for capacity in a multi-antenna channel.

2.1 Existing Model by Saleh and Valenzuela with Angle of Arrival

The recent attention devoted to MIMO wireless communications has motivated renewed interest in the development of accurate channel models capable of simulating realistic MIMO propagation. Previously, Saleh and Valenzuela [3] proposed a model that describes the propagating waves as a set of discrete plane waves. Based on experimental observations, the model groups these waves (or rays) into a few clusters in time. Within each cluster, the amplitude of the rays decays exponentially with time. Similarly, the overall cluster amplitudes decrease exponentially in time. Within the Saleh and Valenzuela (SV) model, the exponential decay is characterized by the time constants Γ and γ for the clusters and rays, respectively. The impulse response of the channel is represented as

$$h(t) = \sum_{m=0}^{\infty} \sum_{k=0}^{\infty} \beta_{km} e^{j\phi_{km}} \delta(t - T_m - \tau_{km}), \tag{2.1}$$

where the sums over m and k represent the clusters and the arrivals with each cluster, respectively. The phase of each ray in 2.1 is given by the term $e^{j\phi_{km}}$, where ϕ_{km}

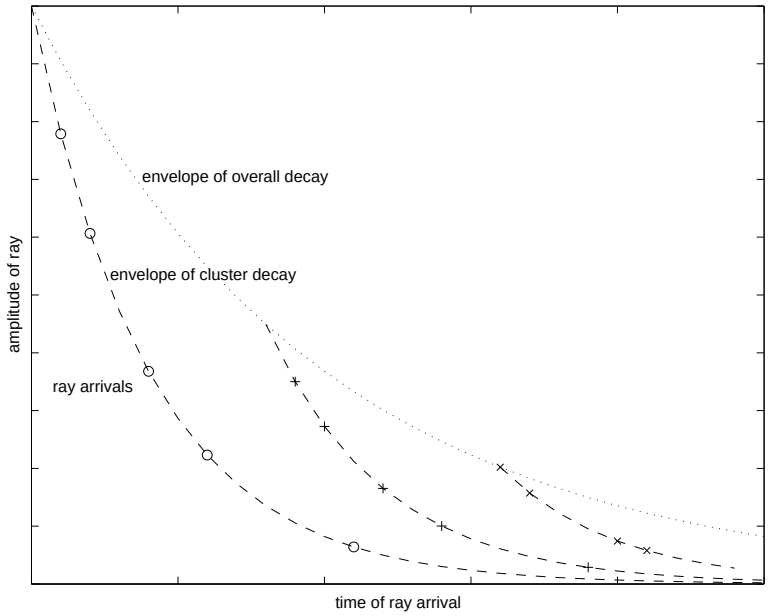

Figure 2.1: Illustration of overall exponential decay of clusters and exponential decay with each cluster

is uniformly distributed. Also, β_{km} represents the amplitude of each ray and is a Rayleigh distributed random variable. The mean square value of β_{km} is given by

$$\overline{\beta_{km}^2} = \overline{\beta^2(T_m, \tau_{km})} \tag{2.2}$$

$$= \overline{\beta^2(0,0)} e^{-T_m/\Gamma} e^{-\tau_{km}/\gamma}, \tag{2.3}$$

where $\overline{\beta^2(0,0)}$ is the mean of the power of the first ray in the first cluster. The arrival time of each cluster, T_m, as well as of each ray within the cluster, τ_{km}, are modeled using double Poisson processes. The probability distribution functions of these parameters are given by

$$p(T_m \mid T_{m-1}) = \Lambda e^{-\Lambda(T_m - T_{(m-1)})} \tag{2.4}$$

$$p(\tau_{km} \mid \tau_{(k-1)m}) = \lambda e^{-\lambda(\tau_{km} - \tau_{(k-1)m}))}, \tag{2.5}$$

where Λ and λ are the cluster and ray arrival rates, respectively. The general behavior of the model is illustrated in Figure 2.1.

In [4], the SV model was extended to the Saleh Valenzuela with Angle (SVA) model by adding the angle of arrival to the model. The impulse response of the SVA modeled channel is represented as

$$h(t,\theta) = \sum_{m=0}^{\infty}\sum_{k=0}^{\infty} \beta_{km} e^{j\phi_{km}} \delta(t - T_m - \tau_{km})\delta(\theta - \Theta_m - \omega_{km})\delta(\alpha - \Delta_m - \kappa_{km}) \quad (2.6)$$

where Θ_m and Δ_m are the mean angles of each cluster at the receiver and transmitter, respectively. ω_{km} and κ_{km} are the ray angles of arrival within a cluster at the receiver and transmitter, respectively. In the SVA model, the ray angle is modeled with a zero mean Laplacian distribution

$$p(\theta) = \frac{1}{\sqrt{2}\sigma} e^{-|\sqrt{2}\theta/\sigma|} \quad (2.7)$$

with σ as the standard deviation.

Using experimental data, Spencer [4]observed that the arrivals are clustered in angle as well as time. The data suggested that the arrival angle of the clusters is uniformly distributed while the angles of the rays within the clusters exhibit a Laplacian distribution. In summary, the SVA model parameters are

- Γ: the cluster arrival decay time constant
- γ: the ray arrival decay time constant
- Λ: the cluster arrival rate
- λ: the ray arrival rate
- β: the amplitude of each arrival
- σ^2: the angular variance.

These SVA model parameters for the fourth floor of the Clyde Building on Brigham Young University campus have previously been explored in [4]. The parameters are given in Table 2.1 and will be used for the SVA channels throughout this thesis.

Table 2.1: SVA model parameters

SVA Parameter	**Value**
angular variance	26°
cluster decay time constant	39 nsec
ray decay time constant	29 nsec
cluster arrival rate	1/(17 nsec)
ray arrival rate	1/(5 nsec)

In more recent work, it was shown that the SVA model is able to accurately predict the behavior of a MIMO system in narrowband indoor channels [11]. However, to date the suitability of the model has not been verified for wideband communication. One goal of this thesis is to examine the behavior of the model for wideband communication and compare this behavior to that of other models.

2.2 SVA Model for Frequency Selective Channels

When applying the SVA model to wideband or frequency selective channels, it is important to properly specify the assumptions made and outline the framework used for this application. This section reviews the assumptions made for narrowband and wideband channel modelling based on the SVA model.

2.2.1 Narrowband Assumptions

When considering using the SVA model to generate wideband channels, we should first review the assumptions made for narrowband modelling so that we can make the appropriate changes. Several such assumptions are inherent in the modelling accomplished to date. First, we assume that the incoming rays are plane waves. It is then reasonable to assume that the magnitude of the signal does not vary over the array. Furthermore, we neglect the time of arrival difference of a ray across the array (except to account for the effect of this on the phase). Thus, from one antenna to another, only the difference in the phase of the ray must be taken into account. Figure 2.2 shows the arrival of one ray at the receive antenna and illustrates the plane wave assumption. The difference in path length for reception at different antennas

leads to a phase change. Since this phase is a function of frequency, in a multipath environment the rays will interfere differently (constructively and destructively) across the frequency band. This leads to the term "frequency selective fading" commonly used in the literature for wideband communications.

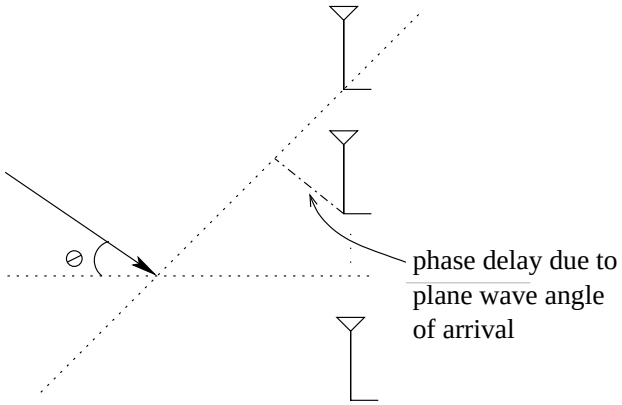

Figure 2.2: Single incoming ray at receive antenna array

For the narrowband case, it is also assumed that the response of the antenna does not change significantly over the frequency band of interest. Since the relative bandwidth is a small fraction of the carrier frequency, this assumption is reasonable.

2.2.2 Wideband Extension

To use the SVA model for wideband channels, several parameters must be accounted for. These parameters include the bulk phase delay between the transmit and receive antenna arrays, the relative phase difference across the antenna aperture for the rays, the wave number as a function of frequency, and the channel gain. The bulk phase delay between the transmit and receive antenna arrays is accounted for with the term

$$\alpha_n = e^{j\omega\tau_n}, \tag{2.8}$$

where τ_n is the time of arrival (relative to the line of sight arrival time) for the n^{th} arrival ray.

The relative phase difference across the antenna aperture is accounted for individually at the receive array and at the transmit array. In a two dimensional propagation model, the relative phase due to wave departure angle at the i^{th} transmit antenna is

$$\rho_{i,n}^{T_x} = e^{jk(\omega)(x_i \cos\theta_n^{T_x} + y_i \sin\theta_n^{T_x})}, \tag{2.9}$$

where $k(\omega)$ is the wave number as a function of frequency, x_i and y_i are the x and y coordinates of the i^{th} transmit antenna (in the coordinate frame of the transmit array), and $\theta_n^{T_x}$ is the departure angle of the n^{th} ray. The relative phase due to wave arrival angle at the j^{th} receive antenna is similarly given by

$$\rho_{j,n}^{R_x} = e^{jk(\omega)(x_j \cos\theta_n^{R_x} + y_j \sin\theta_n^{R_x})}, \tag{2.10}$$

where $\theta_n^{R_x}$ is the arrival angle of the n^{th} ray and (x_j, y_j) is the location of the j^{th} receive antenna.

With the channel gain of the n^{th} ray path given by β_n, the frequency domain representation of the channel is given by

$$H_{ij}(\omega) = \sum_n \beta_n \alpha_n(\omega) \rho_{i,n}^{T_x}(\omega) \rho_{j,n}^{R_x}(\omega), \tag{2.11}$$

where i and j represent the i^{th} receiver and the j^{th} transmitter.

In addition to using all the parameters used in the narrowband SVA model, the wideband implementation of the SVA model also requires the following:

- BW: the bandwidth of interest
- f_o: the carrier frequency.

Though the variation of the amplitude across the frequency response depends greatly on the values for the SVA model parameters in Table 2.1, it is interesting to examine one realization of a frequency selective model. Such an example of an indoor channel for a bandwidth of 25 MHz on a carrier frequency of 2.442 GHz is shown in Figure 2.3.

To determine the behavior of the channel coefficients $H_{i,j}$ with frequency selectivity, consider a single realization of one channel coefficient. Figure 2.3 shows the variation with frequency of this channel coefficient for a bandwidth of 2.442 GHz. As can be seen, even over this relatively narrow bandwidth (roughly 1% fractional bandwidth), considerable variation in the channel coefficient magnitude is apparent.

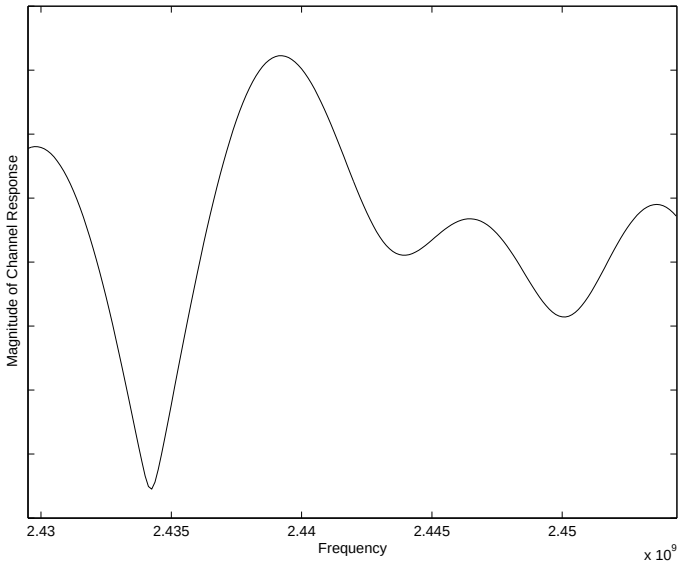

Figure 2.3: One realization of the wideband SVA model

2.3 Indoor Channel Modelling

Recently, different approaches have been taken to simulate wireless multipath propagation channels. One such approach involves placing the scatterers at desired positions and using simple ray tracing to construct the propagation channel model [12], [13]. Such a model provides angle of departure as well as time and angle of arrival for each propagation path. In [13], Molisch places scatterers and uses the information gained about this deterministic channel to generalize the data to a wideband channel. He parameterizes the propagation effects for the wireless channel by using a scatterer

near the base station, a scatterer near the mobile station, a number of far scatterer clusters (each consisting of individual scatterer points), and a number of waveguides and diffraction edges. In [14], Burr used a ray tracing method to simulate several indoor wireless channels. In this thesis, a similar ray tracing model is used to simulate the indoor MIMO channel. The data collected from this model will be compared to the results of the SVA model.

Numerous parameters have been used to characterize wideband channels. Parameters for wideband characterization include coherence bandwidth, mean delay, delay spread, normalized cumulative power, and 90% fixed delay window [15]. Prior studies in channel modeling tend to select a subset of these parameters for investigation. For example, in [16] the coherence bandwidth and RMS delay spread are characterized for indoor propagation at 17 GHz. In this thesis, we will examine all of these broadband channel parameters for a MIMO system operating at 2.442 GHz.

2.3.1 Capacity of the MIMO Channel

For many years, channels characterized by multipath propagation were considered poor channels. However, it is now understood that if multiple antennas are used, a rich multipath environment can lead to increased channel capacity (assuming that the multipath does not degrade the SNR). A significant amount of research has been done to determine this capacity of MIMO channels. Some of the earliest work done by Foschini and Gans [2] revealed that when there is an equal number of antennas at the transmitter and the receiver, such systems have a channel capacity that increases linearly with the number of antennas. In the following, we provide a simple derivation of the achievable capacity of MIMO propagation channels using the water-filling solution.

Water-filling Algorithm Tutorial

The following tutorial is given as background for the wideband water-filling algorithm that is later presented. The water-filling solution can be used to determine the upper bound on capacity for a MIMO system operating in a specific channel

[17]. The objective of this algorithm is to allocate power across the channel so as to maximize the total capacity. This power allocation is subject to the constraint that the sum of the power poured into each channel is less than or equal to P_t, the total power available to the transmitter.

The relative channel strengths and the amount of power to allocate to each channel is determined by knowledge of the (narrowband) channel matrix, H. To determine the relative strength of the orthogonal channels, we first normalize the H matrix such that the average channel gain is unity, or

$$E\{\|H_{ij}\|\} = 1. \tag{2.12}$$

This normalization can be expressed as

$$\frac{\|H\|_F^2}{N_R \cdot N_T} = 1 \tag{2.13}$$

where $\|\cdot\|_F$ represents the Frobenius norm.

We use the eigen decomposition of HH^H to obtain

$$HH^H = U\Lambda U^H,$$

where $UU^H = U^HU = I_{N_R}$ and $\Lambda = \text{diag}\left\{ \begin{array}{cccc} \lambda_1 & \lambda_2 & \ldots & \lambda_{N_R} \end{array} \right\}$ with λ_i as the i^{th} eigenvalue. We assume that the eigenvalues in Λ are ordered such that $\lambda_i \geq \lambda_{i+1}$.

The relative strength of the i^{th} channel is now given by $\frac{SNR}{N_T}\lambda_i$, where N_T is the number of transmit antennas and SNR is the signal to noise power ratio. Since the power allocated to any channel can not be negative, any channel whose inverse channel strength is large enough to require negative power goes unused. Then, if p is the number of positive eigenvalues in Λ, then the channel capacity simplifies to

$$Cap = \sum_{i=1}^{p} log_2 \left(1 + \frac{SNR}{N_T}\lambda_i\right). \tag{2.14}$$

Figure 2.4 illustrates the power allocation for the water-filling algorithm. This will be discussed further in Chapter 4.

The water-filling is done over each non-zero dimension in the channel matrix, H. This is considered water-filling over space or over the channels between antennas. In Chapter 4, we demonstrate a generalized water-filling solution for a frequency selective channel.

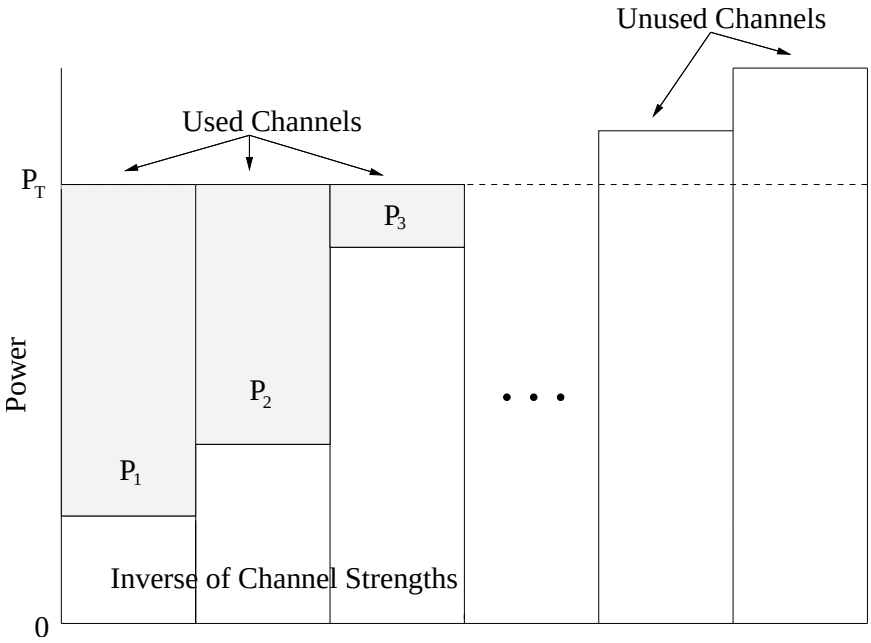

Figure 2.4: A simplified illustration of water-filling

Chapter 3

Maximum Likelihood Channel Estimation

Consider an $N_T \times N_R$ MIMO system, where N_T and N_R represent the number of transmit and receive antennas, respectively. The linear discrete-frequency input-output relationship for this system can be written as

$$\mathbf{y}[f,n] = \mathbf{H}[f]\mathbf{x}[f,n] + \boldsymbol{\eta}[f,n], \tag{3.1}$$

where $\mathbf{x}$ and $\mathbf{y}$ represent the $N_T \times 1$ and $N_R \times 1$ transmit and receive vectors, respectively, $\mathbf{H}$ is the $N_R \times N_T$ channel matrix, and $\boldsymbol{\eta}$ is noise that is assumed throughout to follow a zero-mean, complex Gaussian distribution and to be temporally, spectrally, and spatially white. The variable f, $0 \leq f \leq F-1$, is the discrete frequency index, while n, $0 \leq n \leq N-1$, represents the index of the transmission or *measurement*. It is explicit in (3.1) that the channel is assumed constant over the interval of time required to perform the N measurements (i.e. $\mathbf{H}[f]$ is independent of n).

3.1 Classical Channel Estimation

In the channel estimation problem, we will assume that the receiver knows the transmitted spectrum $\mathbf{x}[f,n]$ as well as the observed response $\mathbf{y}[f,n]$. A straightforward approach to estimating $\mathbf{H}[f]$ is to form the discrete correlation

$$\begin{aligned}
\mathbf{R}_{yx}[f] &= \sum_{n=0}^{N-1} \mathbf{y}[f,n]\mathbf{x}^{\dagger}[f,n] && (3.2)\\
&= \sum_{n=0}^{N-1} \mathbf{H}[f]\mathbf{x}[f,n]\mathbf{x}^{\dagger}[f,n] + \sum_{n=0}^{N-1} \boldsymbol{\eta}[f,n]\mathbf{x}^{\dagger}[f,n] && (3.3)\\
&= \mathbf{H}[f]\mathbf{R}_{xx}[f] + \mathbf{R}_{\eta x}[f], && (3.4)
\end{aligned}$$

where $\{\cdot\}^\dagger$ represents a conjugate transpose. For large N, $\mathbf{R}_{\eta x}[f] = \mathbf{0}$ since the noise is uncorrelated with the signal. Therefore, for N sufficiently large, the solution is

$$\mathbf{H}[f] = \mathbf{R}_{yx}[f]\mathbf{R}^{+}_{xx}[f] \tag{3.5}$$

where the superscript $\{\cdot\}^+$ represents a pseudo-inverse. For modest values of N, this solution is the maximum likelihood (ML) solution under the noise assumptions outlined here.

While this method can lead to very good estimates of the channel, it has the disadvantage that multiple measurements of the same channel are required to obtain good accuracy. In fact, it is noteworthy that the term $\mathbf{x}[f,n]\mathbf{x}^\dagger[f,n]$ has a matrix rank of one. Therefore, $\mathbf{R}_{xx}$ can be full rank only if $N \geq N_T$ (and at least N_T of the vectors $x[f,n]$, $0 \leq n \leq N-1$ are linearly independent). Since the measurement is performed over multiple frequency points, it would be convenient to be able to perform the correlation in the frequency domain, thereby eliminating the need for these multiple measurements in time. Unfortunately, the fact that $\mathbf{H}[f]$ varies with frequency increases the complexity of frequency domain correlation. In the following, we propose a scheme that achieves very good accuracy while requiring only a single measurement in time.

3.2 Basis Function Expansion

Perhaps the simplest approach to performing the correlation in the frequency domain is to simply assume that the channel matrix $\mathbf{H}[f]$ remains constant over a set of $F_B \geq N_T$ frequency samples, where the subscript B indicates the notion of a frequency bin. Then (3.1) can be written over a set of F_B frequency samples as

$$\mathbf{y}[j+bF_B] = \overline{\mathbf{H}}[b]\mathbf{x}[j+bF_B]+\boldsymbol{\eta}[j+bF_B], \qquad 0 \leq j \leq F_B-1, \qquad 0 \leq b \leq B-1 \tag{3.6}$$

where we have dropped the index n as we are only using one channel measurement and the overbar on $\overline{\mathbf{H}}[b]$ simply indicates that the indexing on the transfer matrix is on the bin number b rather than the frequency f. Performing the correlation over

the F_B samples leads to

$$\begin{aligned}
\overline{\mathbf{R}}_{yx}[b] &= \sum_{j=0}^{F_B-1} \mathbf{y}[j+bF_B]\mathbf{x}^{\dagger}[j+bF_B] && (3.7)\\
&= \sum_{j=0}^{F_B-1} \overline{\mathbf{H}}[b]\mathbf{x}[j+bF_B]\mathbf{x}^{\dagger}[j+bF_B] + \sum_{j=0}^{F_B-1} \boldsymbol{\eta}[j+bF_B]\mathbf{x}^{\dagger}[j+bF_B] && (3.8)\\
&= \overline{\mathbf{H}}[b]\overline{\mathbf{R}}_{xx}[b] + \overline{\mathbf{R}}_{\eta x}[b]. && (3.9)
\end{aligned}$$

The ML solution for frequency bin b is therefore

$$\overline{\mathbf{H}}[b] = \overline{\mathbf{R}}_{yx}[b]\overline{\mathbf{R}}^{+}_{xx}[b]. \tag{3.10}$$

The above solution is interesting since it requires only one channel measurement. However, the piecewise-constant representation of the channel transfer matrix frequency variation is somewhat simplistic. With additional effort, however, an improved model for this frequency variation can be included in the computation. Consider again (3.1) without the measurement index n. For computational simplicity, we will examine the signal on the k^{th} receive antenna, or

$$y_k[f] = \mathbf{h}_k[f]\mathbf{x}[f] + \boldsymbol{\eta}_k[f] \tag{3.11}$$

where the $1 \times N_T$ vector $\mathbf{h}_k[f]$ is the k^{th} row of $\mathbf{H}[f]$. We will now expand $\mathbf{h}_k[f]$ using

$$\mathbf{h}_k[f] = \sum_{b=0}^{B-1} p[f-bL]\mathbf{a}_k[b] \tag{3.12}$$

where $p[j]$ is a triangular basis function as shown in Figure 3.1, and $\mathbf{a}_k[b]$ represents a vector of unknown coefficients. The indexing in (3.12) is such that each basis function overlaps with the peak of each function placed at the first (or last) zero sample of the adjacent functions, as shown in Figure 3.2 (b). This form leads to a piecewise-linear representation of the channel matrix, with $\mathbf{a}_k[b]$ representing the value of the channel matrix at the samples corresponding to the peaks in the basis functions. Since p is of length $2L+1$, the total number of bins is

$$B = \left\lfloor \frac{F-L-1}{L} \right\rfloor + 2. \tag{3.13}$$

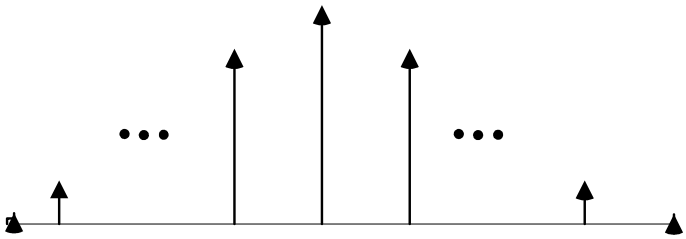

Figure 3.1: Basis function.

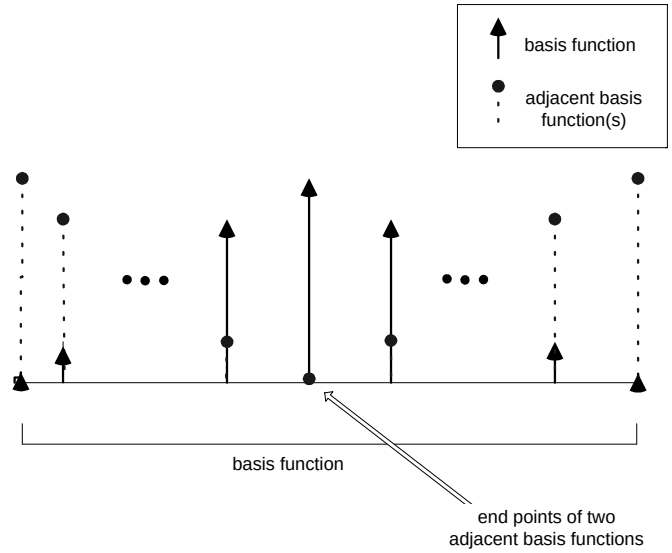

Figure 3.2: Basis function with two adjacent basis functions.

Using this basis expansion, (3.11) can be written as

$$y_k[f] = \sum_{b=0}^{B-1} p[f - bL]\mathbf{a}_k[b]\mathbf{x}[f] + \boldsymbol{\eta}_k[f]. \tag{3.14}$$

If we associate the combination of the original transmit vector and the basis function as the effective transmit spectrum, then the procedure outlined in Section 3.1 suggests performing the operation

$$\begin{aligned}
\tilde{\mathbf{r}}_{k,yx}[b'] &= \sum_{f=0}^{F-1} y_k[f]\mathbf{x}^\dagger[f]p[f - b'L] && (3.15)\\
&= \sum_{b=0}^{B-1} \mathbf{a}_k[b] \sum_{f=0}^{F-1} p[f - bL]\mathbf{x}[f]\mathbf{x}^\dagger[f]p[f - b'L] && (3.16)\\
&+ \sum_{f=0}^{F-1} \boldsymbol{\eta}_k[f]\mathbf{x}^\dagger[f]p[f - b'L] && (3.17)\\
&= \sum_{b=0}^{B-1} \mathbf{a}_k[b]\tilde{\mathbf{R}}_{xx}[b, b'] + \tilde{\mathbf{z}}_k[b']. && (3.18)
\end{aligned}$$

We now form this into a linear system using

$$\begin{aligned}
\tilde{\mathbf{X}} &= \begin{bmatrix} \tilde{\mathbf{R}}_{xx}[0,0] & \dots & \tilde{\mathbf{R}}_{xx}[0,B-1] \\ \tilde{\mathbf{R}}_{xx}[1,0] & \dots & \tilde{\mathbf{R}}_{xx}[1,B-1] \\ \vdots & \vdots & \vdots \\ \tilde{\mathbf{R}}_{xx}[B-1,0] & \dots & \tilde{\mathbf{R}}_{xx}[B-1,B-1] \end{bmatrix} && (3.19)\\
\tilde{\mathbf{A}}_k &= \begin{bmatrix} \mathbf{a}_k[0] & \dots & \mathbf{a}_k[B-1] \end{bmatrix} && (3.20)\\
\tilde{\mathbf{Y}}_k &= \begin{bmatrix} \tilde{\mathbf{r}}_{k,yx}[0] & \dots & \tilde{\mathbf{r}}_{k,yx}[B-1] \end{bmatrix} && (3.21)\\
\tilde{\mathbf{Z}}_k &= \begin{bmatrix} \tilde{\mathbf{z}}_k[0] & \dots & \tilde{\mathbf{z}}_k[B-1] \end{bmatrix}. && (3.22)
\end{aligned}$$

The resulting equation is

$$\tilde{\mathbf{Y}}_k = \tilde{\mathbf{A}}_k\tilde{\mathbf{X}} + \tilde{\mathbf{Z}}_k. \tag{3.23}$$

The unknown coefficients in $\tilde{\mathbf{A}}_k$ can now be approximated using

$$\tilde{\mathbf{A}}_k \approx \tilde{\mathbf{Y}}_k\tilde{\mathbf{X}}^+ \tag{3.24}$$

where we have again neglected the noise term to obtain this single measurement channel estimator. However, this does not represent the ML solution since the noise

term $\tilde{\mathbf{z}}_k$ is no longer spectrally white. We can, however, use a prewhitening filter to obtain the ML solution. In this case, we must construct the effective noise covariance as

$$\begin{aligned}
\tilde{\mathbf{R}}_{k,zz}[b'] &= E\{\tilde{\mathbf{z}}_k^T[b']\tilde{\mathbf{z}}_k^*[b']\} && (3.25)\\
&= E\{\sum_{f=0}^{F-1} p[f-b'L]\mathbf{x}^*[f]\boldsymbol{\eta}_k[f]\sum_{f'=0}^{F-1}\boldsymbol{\eta}_k^*[f']\mathbf{x}^T[f']p[f'-b'L]\} && (3.26)\\
&= \sum_{f=0}^{F-1}\sum_{f'=0}^{F-1}\sigma^2\delta_{ff'}E\{p[f-b'L]\mathbf{x}^*[f]\mathbf{x}^T[f']p[f'-b'L]\} && (3.27)\\
&= \sigma^2\sum_{f=0}^{F-1}E\{p[f-b'L]\mathbf{x}^*[f]\mathbf{x}^T[f]p[f-b'L]\} && (3.28)\\
&= \sigma^2\tilde{\mathbf{R}}_{k,o}[b'], && (3.29)
\end{aligned}$$

where $\{\cdot\}^T$ represents a transpose and we have used the independence of the signal and noise. Using this covariance, a prewhitening filter can be applied to (3.18), leading to the form

$$\tilde{\mathbf{r}}_{k,yx}[b']\tilde{\mathbf{R}}_{k,o}^{-1/2}[b'] = \sum_{b=0}^{B-1}\mathbf{a}_k[b]\tilde{\mathbf{R}}_{xx}[b,b']\tilde{\mathbf{R}}_{k,o}^{-1/2}[b'] + \mathbf{z}_k[b']\tilde{\mathbf{R}}_{k,o}^{-1/2}[b'] \qquad (3.30)$$

which has a noise covariance of $\sigma^2\mathbf{I}_{N_T}$, where $\mathbf{I}_k$ represents a $k\times k$ identity matrix. Using the definition

$$\tilde{\mathbf{R}}_Z = \tilde{\mathbf{R}}_{k,o}^{-1/2}[b']\otimes\mathbf{I}_B \qquad (3.31)$$

leads to

$$\tilde{\mathbf{Y}}_k\tilde{\mathbf{R}}_Z = \tilde{\mathbf{A}}_k\tilde{\mathbf{X}}\tilde{\mathbf{R}}_Z + \tilde{\mathbf{Z}}_k\tilde{\mathbf{R}}_Z. \qquad (3.32)$$

The resulting ML estimate of the unknown coefficients is

$$\hat{\mathbf{A}}_k = \tilde{\mathbf{Y}}_k\tilde{\mathbf{R}}_Z(\tilde{\mathbf{X}}\tilde{\mathbf{R}}_Z)^+. \qquad (3.33)$$

Note that if $(\tilde{\mathbf{X}}\tilde{\mathbf{R}}_Z)$ is square and full-rank, then this estimate is the same as that in (3.24).

It is perhaps important to pause here to emphasize what this estimation procedure has produced. This solution provides the unknown coefficients for the k^{th} row of the channel matrix for all frequency bins ($b = 0$ to $B-1$). The actual elements of the

channel matrix at the frequency samples f are then obtained using these coefficients in (3.12). This leads to a piecewise linear representation of the frequency variation of the transfer matrix elements. To construct the entire matrix using this formulation, the procedure must be performed once for each of the N_R receive antennas.

3.3 ML Solution for Downsampled Data

The technique above constructs the channel matrix using only a single channel measurement that is downsampled in frequency. For comparison purposes, it is interesting to examine the performance obtained when using multiple measurements in time while downsampling in frequency. In this case, we will place the data into frequency bins windowed by the function $p[j]$ used above. The linear input-output relationship for a single bin of index b and measurement of index n is given as

$$\begin{aligned} \mathbf{y}_o[b,n] &= \sum_{f=0}^{F-1} p[f-bL]\mathbf{y}[f,n] && (3.34) \\ &= \sum_{f=0}^{F-1} p[f-bL]\mathbf{H}[f]\mathbf{x}[f,n] + \sum_{f=0}^{F-1} p[f-bL]\boldsymbol{\eta}[f,n]. && (3.35) \end{aligned}$$

Since the window function is non-zero only over a small subset of the F frequency samples, we will assume that the transfer matrix is constant over this range, or

$$\mathbf{H}[f] \approx \mathbf{H}_o[b] \qquad \text{for } f \text{ in the } b^{th} \text{ bin.} \tag{3.36}$$

We may then write

$$\begin{aligned} \mathbf{y}_o[b,n] &= \mathbf{H}_o[b]\sum_{f=0}^{F-1} p[f-bL]\mathbf{x}[f,n] + \sum_{f=0}^{F-1} p[f-bL]\boldsymbol{\eta}[f,n] && (3.37) \\ &= \mathbf{H}_o[b]\mathbf{x}_o[b,n] + \boldsymbol{\eta}_o[b,n]. && (3.38) \end{aligned}$$

Now, we form the linear system

$$\begin{aligned} \mathbf{R}_{o,yx}[b] &= \sum_{n=0}^{N-1} \mathbf{y}_o[b,n]\mathbf{x}_o^\dagger[b,n] && (3.39) \\ &= \mathbf{H}_o[b]\sum_{n=0}^{N-1} \mathbf{x}_o[b,n]\mathbf{x}_o^\dagger[b,n] + \sum_{n=1}^{N} \boldsymbol{\eta}_o[b,n]\mathbf{x}_o^\dagger[b,n] && (3.40) \\ &= \mathbf{H}_o[b]\mathbf{R}_{o,xx}[b] + \mathbf{R}_{o,\eta x}[b]. && (3.41) \end{aligned}$$

The ML solution is therefore

$$\mathbf{H}_o[b] = \mathbf{R}_{o,yx}[b]\mathbf{R}^{+}_{o,xx}[b]. \tag{3.42}$$

3.4 Channel Probing

The first step in obtaining the channel transfer matrix for multi-antenna systems involves performing channel probing measurements. To distinguish the signal on one antenna from that on another, these codes should have good correlation properties. Codes such as those explained in section 4.1 are good candidates and are thus used here to compare the different channel estimation techniques.

3.5 Comparison of Channel Reconstruction Methods

It is interesting to compare the performances of the channel reconstruction methods described above. Figures 3.3, 3.4, and 3.5 illustrate the ability of the multi-measurement method without averaging, the multi-measurement method with averaging and the single measurement method, respectively. The plots show the actual channel with the channel estimation to show that the estimator tracks the channel very well.

SNR is used in this work as defined in section 4.3.1. The root mean square error is calculated at all applicable receive antennas at once for each of these methods by

$$E = \left[\frac{1}{N_R N_T B} \sum_{b=1}^{B} \sum_{n=1}^{N_T} \sum_{m=1}^{N_R} \left(\frac{H(m,n,b) - \tilde{H}(m,n,b)}{H(m,n,b)} \right)^2 \right]^{\frac{1}{2}} \tag{3.43}$$

where N_R represents the number of receive antennas, N_T represents the number of transmit antennas and B represents the number of frequency bins. Note that with the multi-measurement method the reconstruction is performed at one receive antenna at a time which makes N_T equal one for equation 3.43.

Figure 3.6 illustrates the ability of the different reconstruction methods in estimating the channel of interest. At lower SNR, the single measurement estimation method generally estimates the channel with slightly lower SNR than either of the

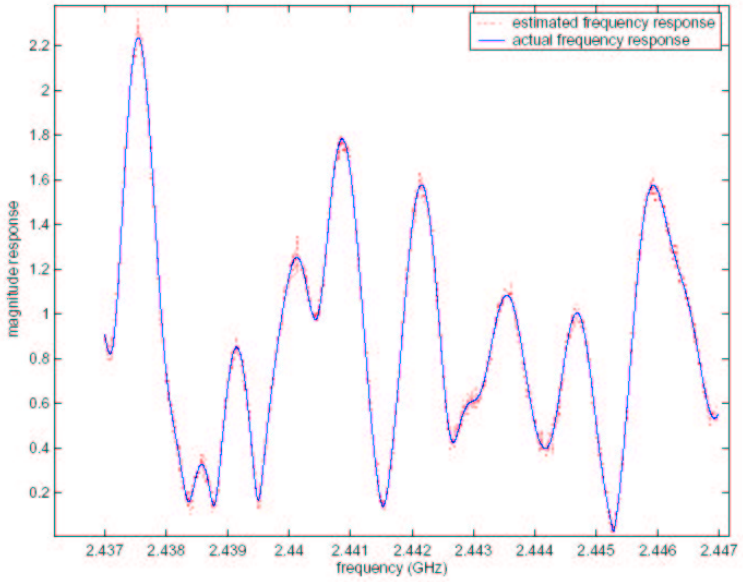

Figure 3.3: Multi-measurement channel estimation with no averaging.

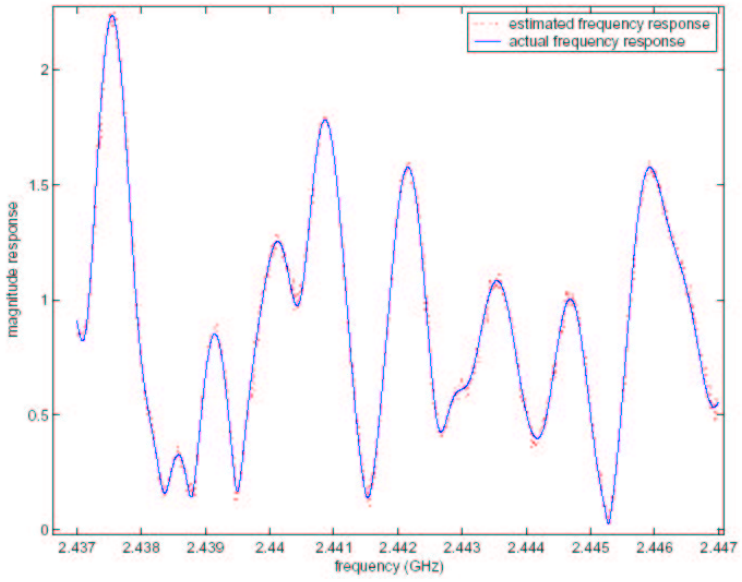

Figure 3.4: Multi-measurement channel estimation with averaging.

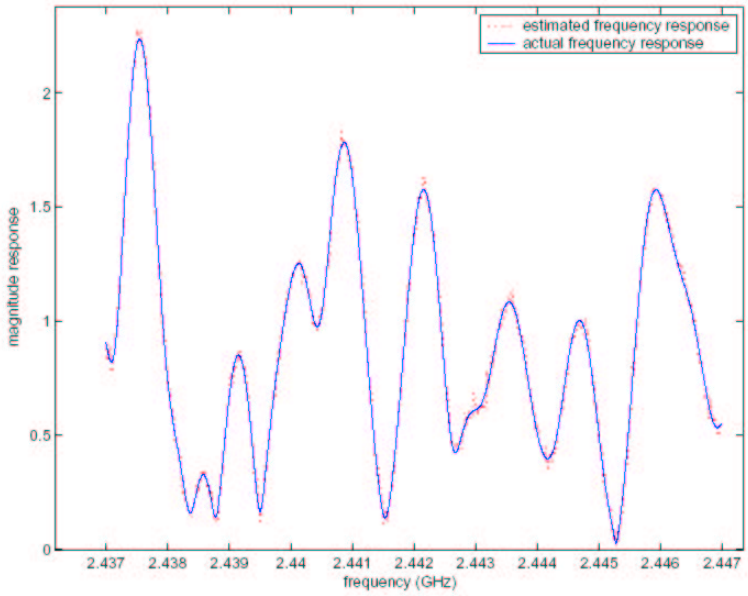

Figure 3.5: Single measurement channel estimation with averaging.

multi-measurement estimation methods. At higher SNR, the single measurement estimation method performs similarly to the multi-measurement without averaging.

For a fair comparison of the different reconstruction methods, all estimates are for a 4x4 MIMO channel that is divided into 1,000 frequency bins for estimation purposes. The channels used for the reconstruction are generated using the raytracing model (see section 4.1) where the center frequency is 2.442 GHz for the 10 MHz band. Where averaging is done across bins (as explained in section 3.2), each point shown in figure 3.6 is the average of RMS errors from multiple channel reconstructions. The single measurement channel estimator and the multi-measurement channel estimators are performed with 10 and 15 channel measurements, respectively.

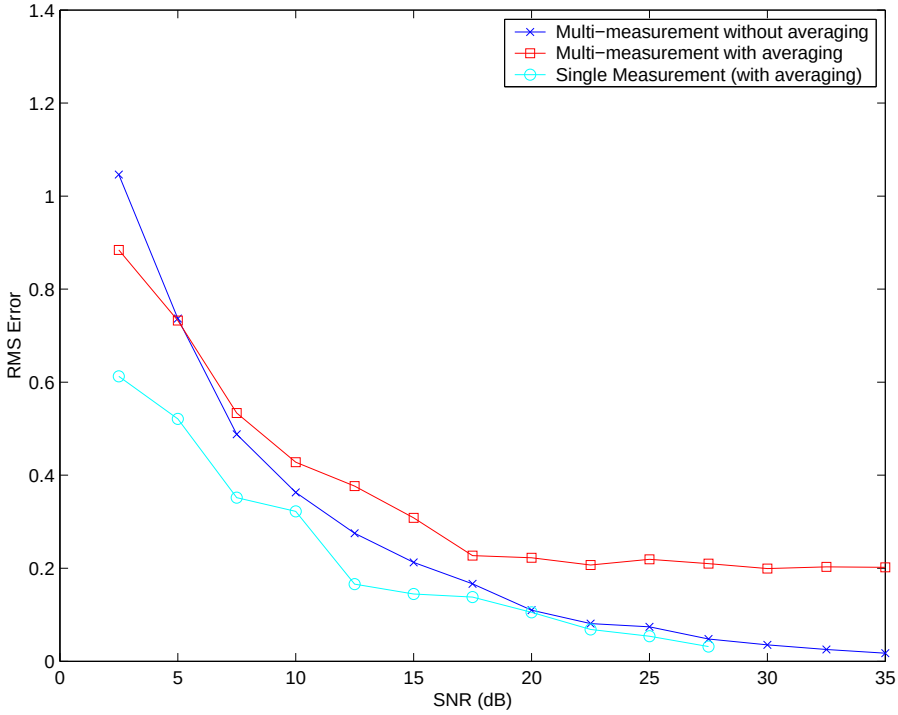

Figure 3.6: Comparison of Estimations Methods over varying SNR.

Chapter 4

Wideband Channel Simulations and Analysis

As stated in Chapter 1, the original goal of this thesis involved measurement of wideband MIMO channel transfer matrices and comparing the results with those generated with the SVA model. However, due to difficulty with the implementation of the hardware probing platform, we will instead utilize an electromagnetic ray tracing system as a substitute to the measurements.

This chapter presents the data simulations used to analyze wireless wideband MIMO channels. The ray tracing tool used to generate data from which MIMO channels are estimated using the single measurement algorithm is presented in section 3.2. Parameters for wideband MIMO channels are also presented and used to compare the estimated channels with those generated using the SVA model.

4.1 Simulated Wideband Channel

The software used for simulating the wideband channel is an electromagnetic ray tracing tool developed at Bell Laboratories for designing indoor and campus-sized ("micro-cell") wireless systems. This software system, called Wireless System Engineering (WiSE), was designed to simulate a wireless channel given a database containing scatterer locations and composition (walls, doors, drinking fountains, etc.), electromagnetic parameters such as frequency, and locations of the transmit and receive antennas. WiSE was designed to determine the best location for a base-station transceiver from the simulated channel's performance.

For this research, the ray tracing portion of the WiSE system is used to simulate indoor wireless channels on the fourth floor of the Clyde building on Brigham

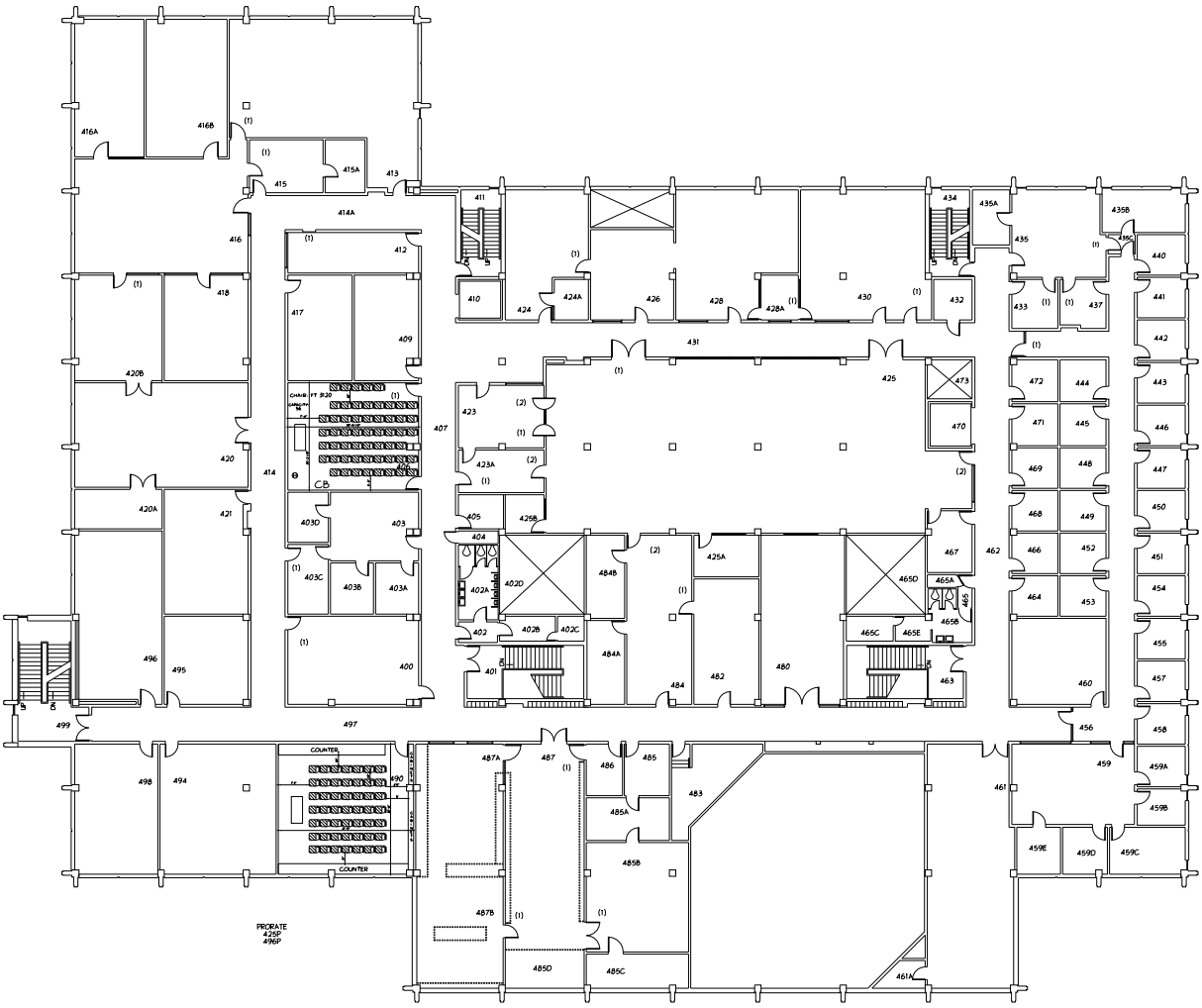

Figure 4.1: Illustration of the fourth floor of the Clyde Building

Young University, as depicted in Figure 4.1. The ray tracing model allows the user to input a database of the scatterers and the type of material for each scatterer. Permanent structures from the fourth floor of the Clyde building were used for the wireless indoor environment, including walls, staircases, drinking fountains, a mechanical shaft, lockers and window frames. The simulations were conducted for rooms 400, 494, 495, 496 and 498 with the transmit and receive arrays in different rooms.

Electrical parameters within the ray tracing model include the transmit power, the location of the transmit and receive antennas and the noise floor (any ray that arrives at the receiver with less than this specified amount of power is ignored). The

tool then supplies the angle of departure and arrival (in azimuth), the channel gain, the time of arrival (relative to the line of sight arrival), and the length of the path travelled for each ray. This multipath ray information is used to generate the channel matrix in exactly the same manner as when the SVA model is used to obtain multipath parameters. To account for the frequency selectivity of the simulated channel, we apply the same assumptions made for the wideband extension of the SVA model in section 2.2.2.

4.2 Channel Probing

A potential waveform for probing the frequency-dependent wireless channel is a frequency chirp. This waveform provides a very flat spectrum over the chirp bandwidth, a property not shared with code-based channel probing waveforms. The frequency of the chirp increases linearly in time with a waveform described by

$$x(t) = e^{j(bt^2+\omega_0 t)}, \tag{4.1}$$

where b controls the chirp rate. Figure 4.2 shows the real part of the spectrum of four different chirps constructed with different values of b. The spectrum of the chirp, expressed as

$$X(\omega) = \sqrt{\frac{\pi}{-jb}} e^{-j\frac{(\omega-\omega_0)^2}{4b}}, \tag{4.2}$$

clearly has a magnitude that is constant in frequency.

Because the chirp spectrum is simulated over a finite frequency band, the spectrum from (4.2) is windowed with a rectangular function in the frequency domain. However, another window could be chosen to obtain a different time domain representation of the signal if desired.

4.3 Analysis of Frequency Selective Channels

The following section presents some estimated channels along with channel analysis to compare some of the wideband channel properties from the ray tracing system with those of the SVA model. To compare the simulated data channels with

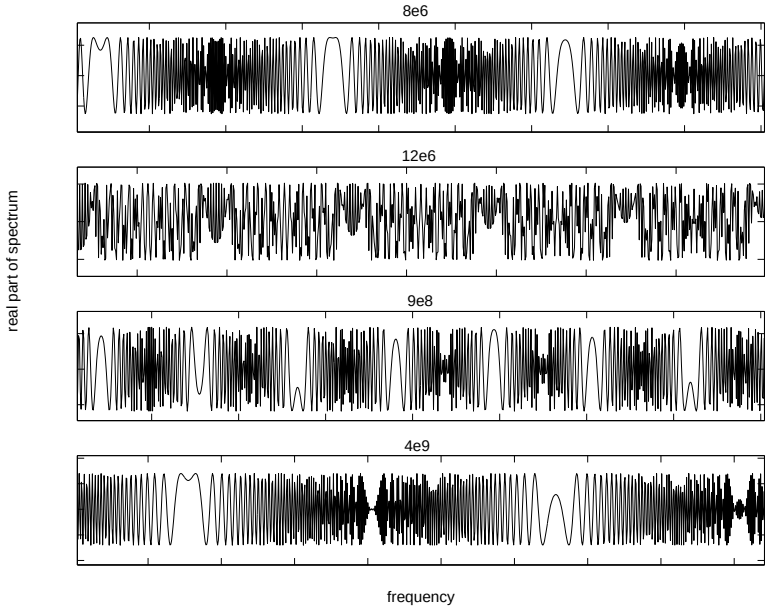

Figure 4.2: Real part of four different chirp spectra, X(ω)

those from the SVA model, parameters such as the channel capacity, coherence bandwidth, power delay profile, delay spread, and delay interval are used.

4.3.1 Wideband MIMO Channel Capacity

One well established method for estimating the narrowband channel capacity is by use of the water-filling algorithm as discussed in section 2.3.1. In order for the solution to estimate the capacity bound on a frequency selective channel, the water-filling algorithm must water-fill over both space and frequency. One logical approach to wideband water-filling is to break up the wideband channel into frequency flat sub-channels and perform narrowband capacity estimates on each of the subchannels as illustrated in Figure 4.3.

If the wideband channel is divided into F_s subchannels, then the receive signal can also be broken into F_s frequency bins, as represented by

$$\mathbf{y}_i = H_i \mathbf{s}_i + \mathbf{z}_i,$$

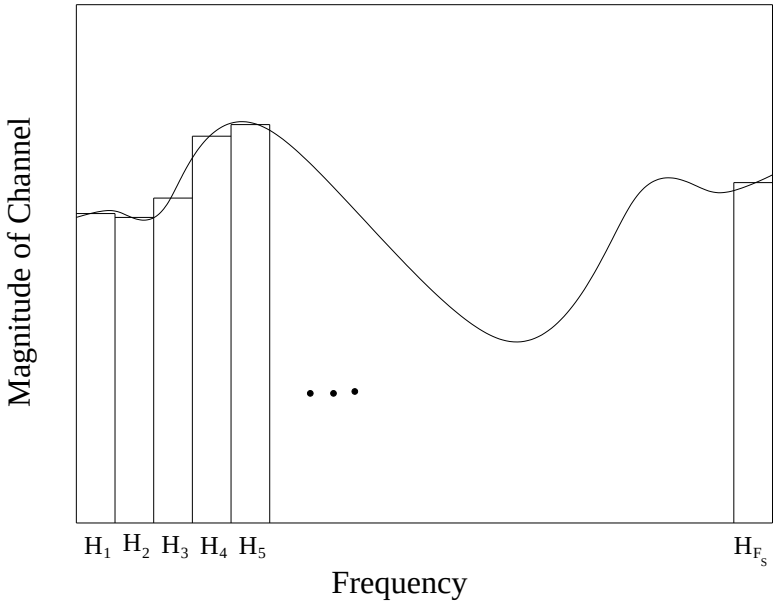

Figure 4.3: Wideband channel subdivided into narrowband channels

where $\mathbf{y}_i$ and $\mathbf{s}_i$ are the receive and transmit data, respectively, for the i^{th} frequency bin. Also for the i^{th} frequency bin, H_i is the channel matrix and $\mathbf{z}_i$ is the noise, where $i = \{1, 2, \ldots, F_s\}$. Each narrowband channel matrix, H_i, is then stacked to form the block-diagonal matrix

$$H_{block} = \begin{pmatrix} H_1 & 0 & \ldots & 0 \\ 0 & H_2 & & \\ \vdots & & \ddots & \vdots \\ 0 & & \cdots & H_{F_s} \end{pmatrix}. \tag{4.3}$$

From H_{block}, the capacity of the wideband channel can be found in a way similar to that for the narrowband. To account for the number of frequency bins, the channel must be normalized as described below.

Power Normalization

In order to have consistent channel parameters for comparing results from different realizations, some normalization must be performed on the channel and the

SNR. First, the wideband channel is normalized such that

$$\frac{\|H_{block}\|_F^2}{N_R \cdot N_T \cdot F_s} = 1. \tag{4.4}$$

Notice that this normalization differs from the narrowband channel normalization in (2.13) by a factor of F_s.

To define the normalization of SNR, the transmit power and noise power must be defined. The total power transmitted from all transmit antenna is normalized such that

$$E\{\|X\|_F^2\} = E_s \tag{4.5}$$

where E_s is the total transmitted power. Because the expectation is difficult to manage, the estimate for the transmit power normalization is taken as

$$\|X\|_F^2 = E_s. \tag{4.6}$$

For this research, SNR (given as a linear ratio) is simply defined as

$$SNR = \frac{E_s}{Z_T}, \tag{4.7}$$

where Z_T is the total noise power seen from all the receive antennas. This noise power is defined such that

$$E\{\|Z\|_F^2\} = Z_T, \tag{4.8}$$

where once again, the expectation for a single realization is estimated as

$$\|Z\|_F^2 = Z_T. \tag{4.9}$$

These definitions of E_s, Z_T and SNR are SIMO (Single Input Multiple Output) in that the SNR is dependent upon the number of receive antennas. However, for the above definition of SNR, the noise at the receive array increases for each additional receive antenna.

An alternate definition for SNR is

$$SNR = \frac{E_s}{(\frac{Z_T}{N_R})}, \tag{4.10}$$

where N_R is the number of receive antennas. This definition suggests more of a SISO (Single Input Single Output) SNR. The SISO definition of SNR allows the SNR to stay constant with any number of receive antennas and thus allows for comparison of MIMO parameters at different array sizes. However, it should also be noted that the difference between the SISO SNR and the SIMO SNR is a scaling of the linear SNR. Furthermore, since all computations here are for the same number of receive antennas ($N_R = 4$), the results can all be compared fairly using the definition of (4.10).

Capacity Results

As illustrated in Figure 2.4, the SNR plays an integral role in determining the capacity of the channel. In order to explore the channel capacity for different SNR values, simulations were run to estimate the channel capacity at an SNR of 50 dB and an SNR of 25 dB.

To illustrate the capacity of the channels simulated on the fourth floor the Clyde Building on Brigham Young University campus, the CCDF (complementary cumulative distribution function) for the capacity is given in Figure 4.4 for $SNR =$ 50 dB and in Figure 4.5 for $SNR = 25$ dB. From Figure 4.4 it can be seen that at $SNR = 50$ dB there is 90% certainty that there is at least 25 bps/Hz of capacity available from the channel. Likewise, at $SNR = 25$ dB there is 90% certainty that there is at least 4.45 bps/Hz of capacity available from the channel.

The ray tracing system yields channels whose capacities are between 5% and 7% higher than the capacity of the channels from the SVA model. The slightly higher capacity bound is most likely due to the wider spread in the distribution of the angle of arrival and the distribution of the angle of departure. Other than the difference in the angles of arrival and departure, the ray tracing system and the SVA model have very similar ray parameters.

4.3.2 Coherence Bandwidth

Coherence bandwidth is the approximate maximum bandwidth or frequency interval over which two frequencies of a signal are likely to experience comparable or

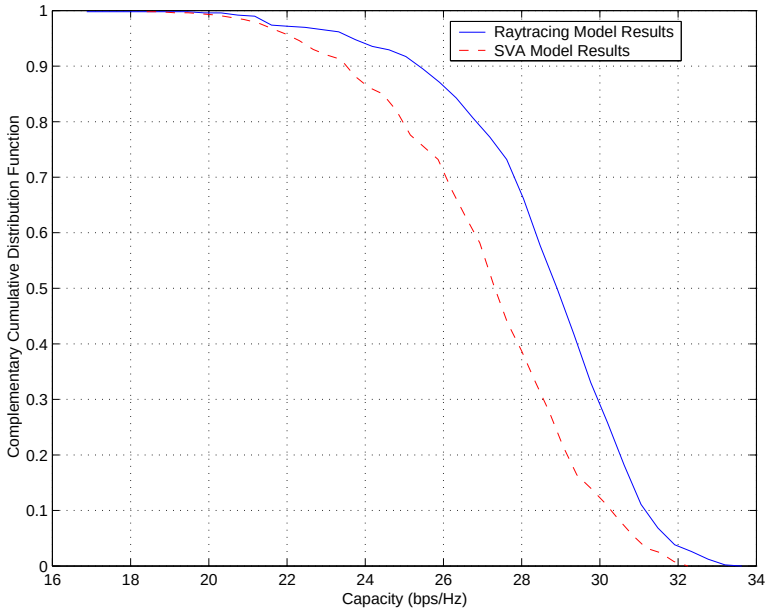

Figure 4.4: Complementary cumulative distribution function of the capacity for the 4x4 MIMO channel at SNR = 50.

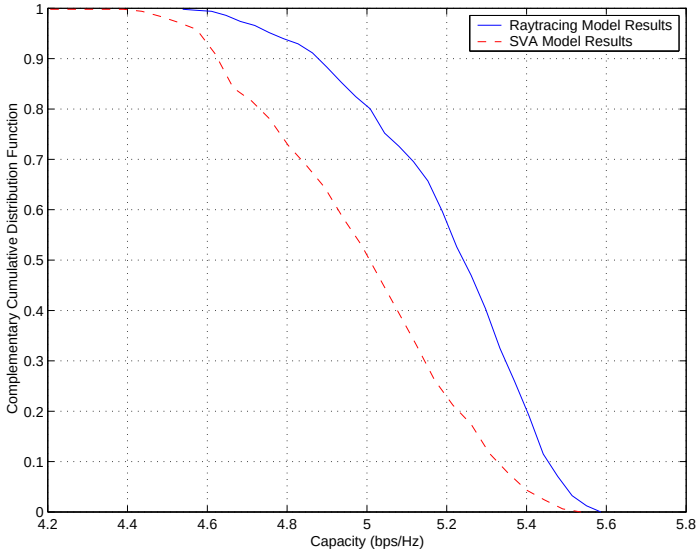

Figure 4.5: Complementary cumulative distribution function of the capacity for the 4x4 MIMO channel at SNR = 25.

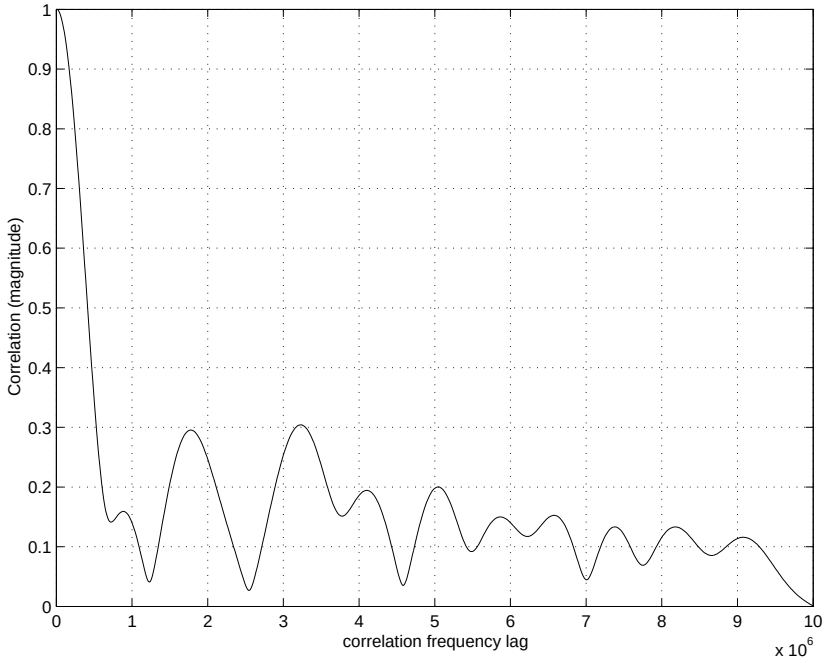

Figure 4.6: The frequency correlation function used to compute coherence bandwidth

correlated amplitude fading. Frequencies within a coherence bandwidth of one another tend to all fade in a similar or correlated fashion. Two values for the correlation will be used to study the multipath channels: 90% coherence bandwidth, $B_{0.9}$, and 50% coherence bandwidth, $B_{0.5}$.

Coherence bandwidth is computed by use of the auto-correlation across frequency for the channel, defined as

$$R_H[k,l] = E\{H[k]H^*[l]\}. \tag{4.11}$$

For 90% coherence bandwidth, $B_{0.9}$ is the bandwidth over which R_H remains greater than or equal to .9. One realization of the frequency correlation function for a highly frequency selective channel is shown in Figure 4.6, where the 90% and the 50% coherence bandwidths are $B_{0.9} = 170$ kHz and $B_{0.5} = 420$ kHz, respectively.

The coherence bandwidth given by the ray tracing solution is very similar to that obtained from the SVA model channels, as shown in the CCDFs of Figures 4.7 and 4.8. With 90% certainty, the channels from the ray tracing and the SVA model

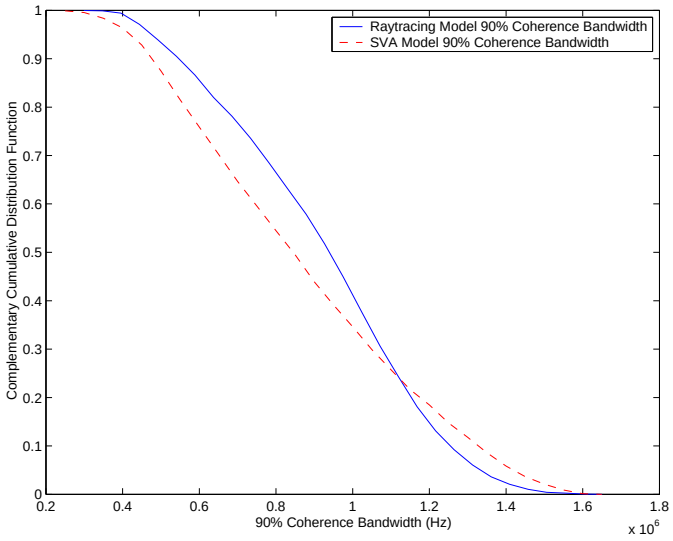

Figure 4.7: Complementary cumulative distribution function for coherence bandwidth of 90%

both show that $B_{0.9}$ is approximately 500 kHz, while $B_{0.5}$ is approximately 2.5 MHz. For both $B_{0.9}$ and $B_{0.5}$, the ray tracing algorithm yields a slightly higher coherence bandwidth. To illustrate some of the statistics concerning the coherence bandwidth, the complementary cumulative distribution functions for $B_{0.9}$ and $B_{0.5}$ are given in Figures 4.7 and 4.8.

4.3.3 Time Domain Parameters

The multi-path delay spread is defined as the time spread between the arrival of the first and last components of the multipath signal as seen by the receiver. The delay spread is most easily computed by means of the delay-power spectral density or the power delay profile.

Power-Delay Profile

The power-delay profile (referred to hereafter as simply the delay profile) is the expected power per unit of time received with a certain excess delay. As shown later, the delay profile will be derived for this work from the frequency response of the

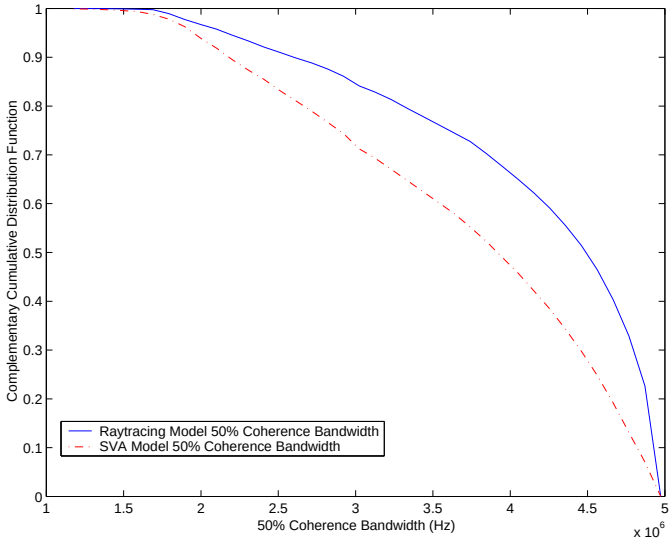

Figure 4.8: Complementary cumulative distribution function for coherence bandwidth of 50%

channel. The delay profile can also be used to determine to what extent the channel fadings are correlated at two different frequencies and can be obtained by averaging a large set of impulse responses. Fortunately, the baseband channel impulse response (and thereby the delay-power profile) is obtainable via the inverse Fourier transform of the frequency domain transfer function of the channel.

Perfect resolution of the delay profile would allow us to see the arrival of individual (or the sum of multiple) rays at any moment in time. However, because only a finite frequency bandwidth is used to probe the channel, the frequency domain windowing results in reduced resolution in the time domain. If the i^{th} incoming ray is represented by

$$ray[i] = \beta[i]e^{j\omega\tau[i]}, \tag{4.12}$$

where $\tau[i]$ is the arrival time of $ray[i]$, then the windowing in the frequency domain causes the time domain response of each ray to become a sinc function as represented

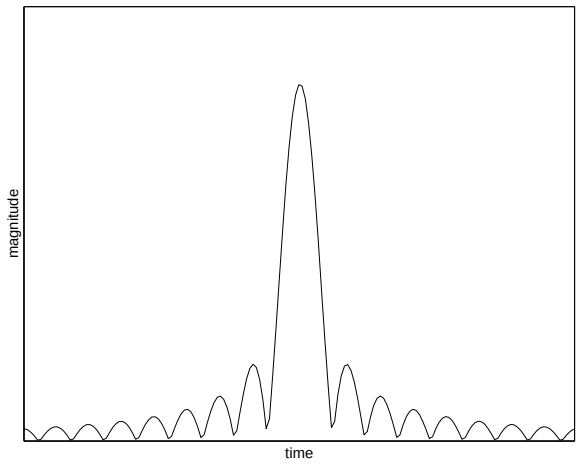

Figure 4.9: A single time domain arrival ray that has been windowed in the frequency domain

by

$$sinc_k[i] = IFT\{ray[i]\} \tag{4.13}$$

$$= IFT\{\beta[i]e^{j\omega\tau[i]}\}, \tag{4.14}$$

where IFT represents the inverse Fourier transform. This sinc function is illustrated in Figure 4.9. It is not possible to perfectly resolve the individual rays since the magnitude-delay profile will contain the sum of the different sinc representations of the impulse responses. The time domain response from all the rays results in the magnitude-delay profile as represented by

$$M_k = \sum_{i=1}^{r} sinc_k[i], \tag{4.15}$$

where r is the number of incoming rays. To illustrate this point, one simplified channel realization with six arrival rays at the receiver is shown in Figure 4.10.

Finally, the magnitude-delay profile is the sum of all the windowed arrival rays. The delay profile is obtained by the square of the magnitude-delay profile as given by $P_k = M_k^2$ for the k^{th} time index. Figure 4.11 shows the delay profile from the windowed rays in Figure 4.10. From this delay profile, it can be seen that as the

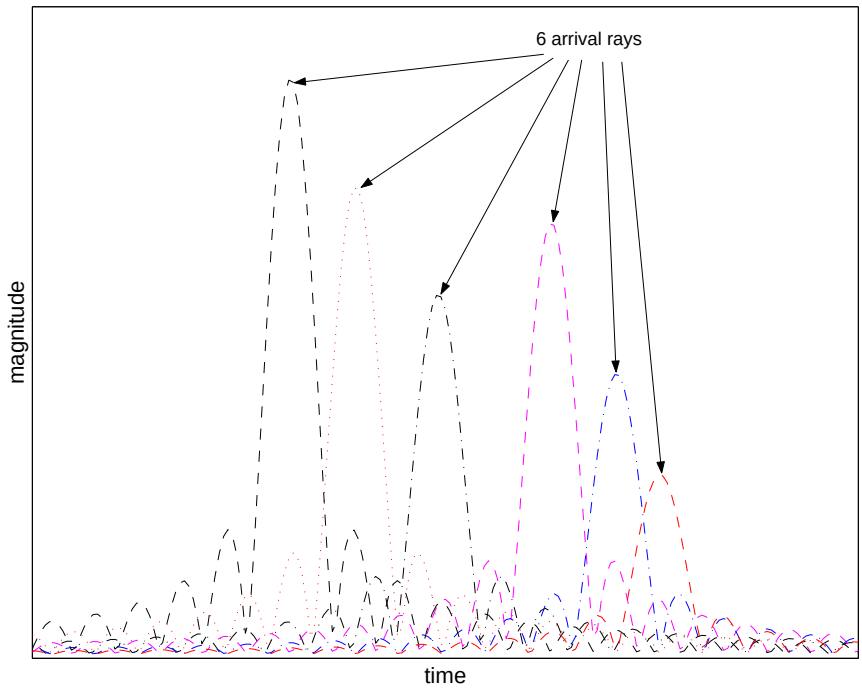

Figure 4.10: Six arrival rays that have been windowed in the frequency domain

arrival times of two rays get closer, it becomes increasingly difficult and eventually impossible to distinguish the two rays from each other. Some added resolution (or at least interpolation) is gained by zero-padding the frequency domain channel transfer function before performing the inverse Fourier transform. Fortunately, for the time-domain parameters used to describe the MIMO channels in this thesis, the resolution of individual times of ray arrival is not necessary.

RMS Delay Spread

One useful parameter found from the delay profile which we will use to further compare the ray tracing computed channels with the SVA model generated channels is the RMS delay spread. The RMS delay spread is the standard deviation (or root-mean-square) value of the delay of rays, weighted proportional to the energy in the rays. To find the RMS delay spread, we start by computing the mean delay. If P_k is

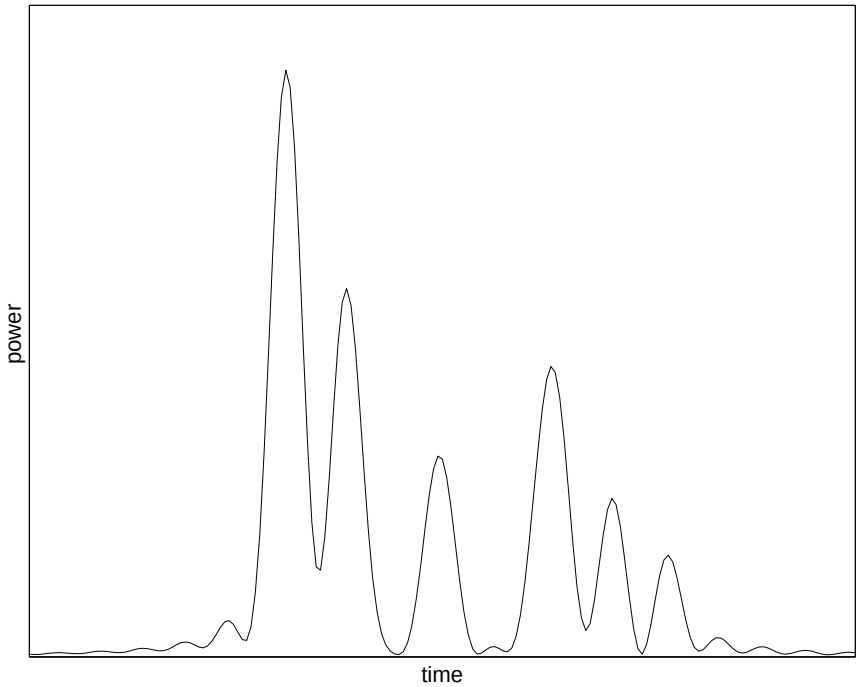

Figure 4.11: Delay Profile from six arrival rays that have been windowed in the frequency domain

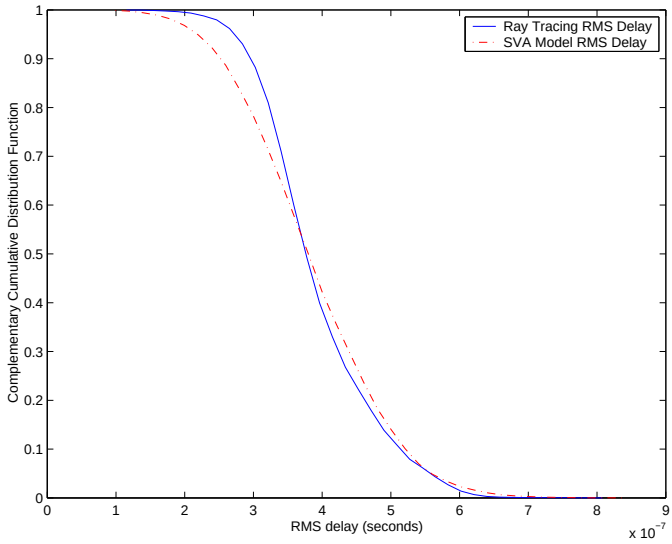

Figure 4.12: Complementary cumulative distribution function for RMS delay spread

the power-delay profile of the k^{th} time index, the mean delay is defined as

$$\tau_0 = \frac{1}{P_T} \sum_{k=0}^{N} \tau_k P_k, \tag{4.16}$$

where

$$P_T = \sum_{k=0}^{N} P_k.$$

The RMS delay spread is then defined as

$$\tau_{RMS} = \sqrt{\frac{1}{P_T} \sum_{k=0}^{N} (\tau_k - \tau_0)^2 P_k}. \tag{4.17}$$

For the data simulated using the ray tracing system and the SVA model, the complementary cumulative distribution (CCDF) function for τ_{RMS} is shown in Figure 4.12. Typical values from the simulated data include values between about .3 μsec and .5 μsec. There is a slightly larger spread in the values of RMS delay spread for SVA model, but agreement between the ray tracing system and the SVA model is extremely good.

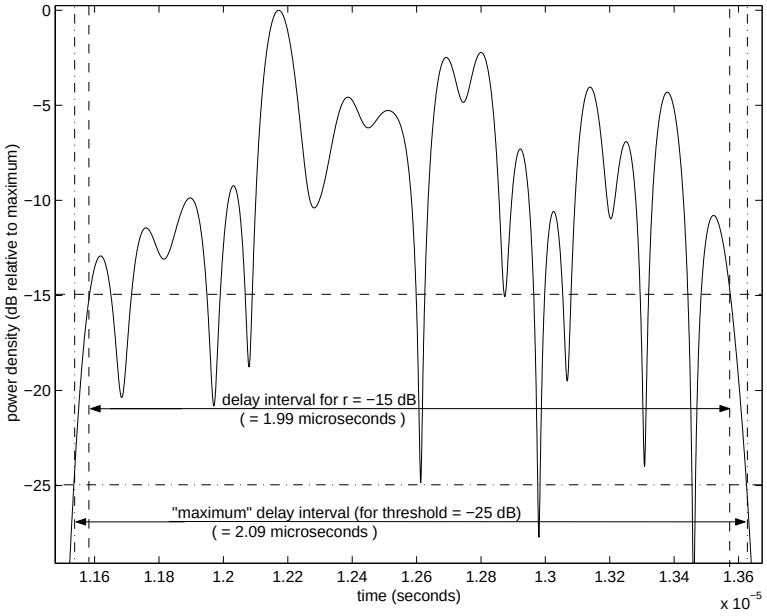

Figure 4.13: Illustration of delay intervals on a power-delay profile

Delay Interval and Maximum Delay Interval

Because the mean delay and the RMS delay spread are not sufficient to describe all the important characteristics of the wideband channel, two additional time-domain parameters are computed from the power-delay profile to help describe the channel. The delay interval is used to describe the duration in time between the points where the power-profile first crosses a threshold point r dB below its maximum to where it falls below that threshold for the last time. For the highly frequency selective channel depicted in Figure 4.13, the delay interval for a drop in power of 15 dB, $\tau_{15} = 1.99$ μsec. As noted in the discussion on the computation of delay profile, due to necessary windowing of the frequency domain transfer function, the delay profile gives a slightly higher value for the delay interval, than what would be obtained assuming infinite bandwidth available for probing.

To illustrate the delay interval for the channels simulated on the fourth floor of the Clyde Building, the CCDF for delay interval with $r = 15$ dB is given in Figure 4.14. The delay interval for the ray tracing simulations and the SVA model channels

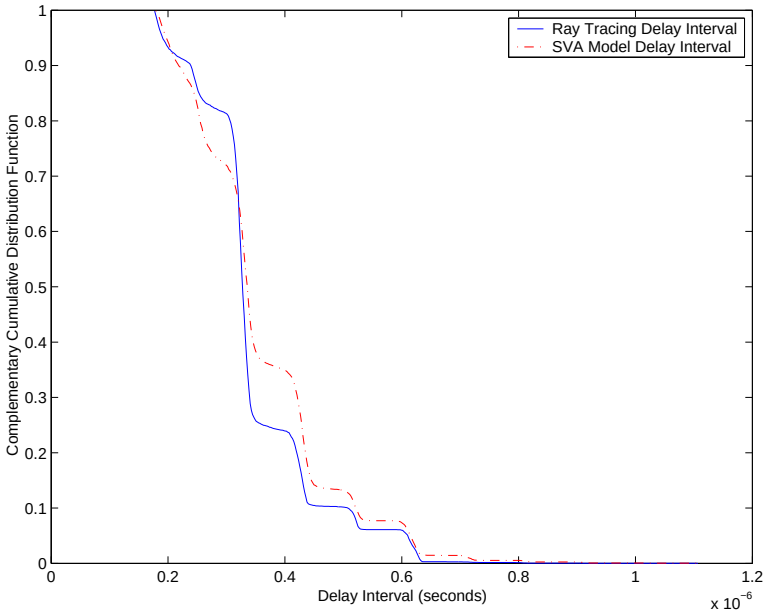

Figure 4.14: Complementary cumulative distribution function for delay interval

have very good agreement and both give over 90% confidence that the delay interval is at least 0.2 μsec.

Maximum Delay Interval

Another parameter of interest is the maximum delay interval, which is defined as the total time interval during which reflections with significant energy arrive. This is similar to the delay interval except that it is used to specifically describe the time delay for all the energy to arrive at the receiver. With an appropriate threshold set above noise level, the maximum delay spread is the difference in time between the points where the power-delay profile first crosses the threshold and point where the power-delay profile crosses the threshold for the last time. A highly frequency selective channel is used in Figure 4.13 to illustrate the maximum delay time spread.

To compare the maximum delay interval for the simulated ray tracing channels and SVA model channels, the CCDF for maximum delay interval is given in Figure 4.15 with the power threshold cutoff was set at -25 dB. As illustrated by the CCDF

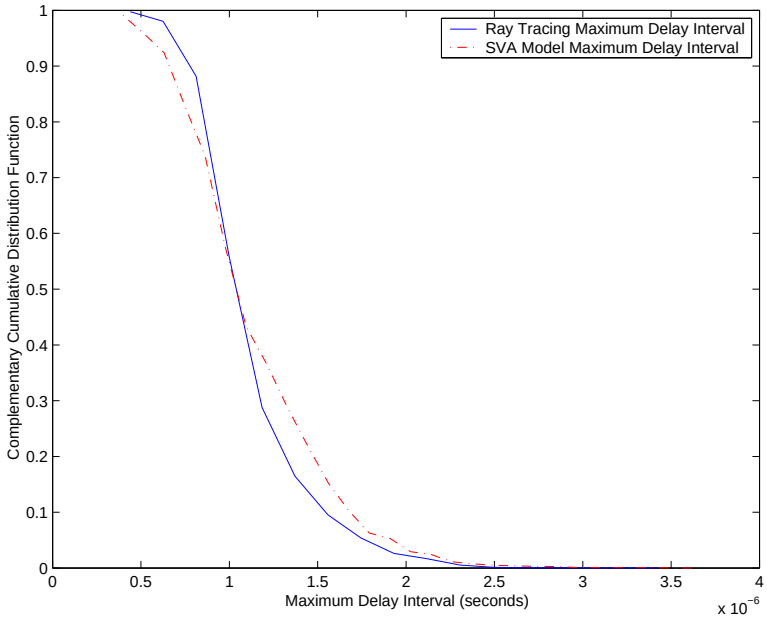

Figure 4.15: Complementary cumulative distribution function for maximum delay interval

of τ_{max}, 90% of the channels generated using the SVA model have a maximum delay interval of at least .66μsec while the ray tracing simulations show a slightly higher maximum delay interval at .78μsec. As noted from the RMS delay spread, the SVA model gives a larger spread of values for the maximum delay interval. Once again, the two models give very similar results for this parameter.

4.4 Summary of Results

The results presented in this chapter show the capability of the SVA model to model wideband MIMO communication channels. Comparison of parameters used to characterize the channels shows good agreement between the SVA model and simulated data from the electromagnetic ray tracing system. The wideband channel capacity comparisons show that the SVA model and the ray tracing system give channels whose wideband capacity is within 5% to 7% of each other. In general, the ray tracing system yields the slightly higher capacity.

The two models also give good agreement for the 90% and 50% coherence bandwidths, with about a 10% difference between the SVA model and the ray tracing simulations for coherence bandwidth. It is interesting to note that for both channel algorithms, the 90% coherence bandwidths are close to 500 kHz.

For the time domain parameters presented in section 4.3.3, the SVA model proves to be in very good agreement with the channels found from the electromagnetic ray tracing simulations. The SVA model gives a slightly wider distribution of values for the RMS delay spread and maximum delay interval. The channels from SVA model and the ray tracing system both yield an RMS delay with 90% certainty of approximately .275 μsec. The maximum delay of both algorithms also has good agreement with maximum delay at approximately .7 μsec with 90% certainty.

Chapter 5

Conclusion

Broadband multiple-input multiple-output (MIMO) wireless channel modelling has been explored to compare simulated channels from a ray tracing system with channels from an SVA model. Chapter 2 presented the narrowband SVA model along with the assumptions made in applying it to estimate wideband MIMO channel matrices.

Chapter 3 presented two signal processing algorithms for obtaining wideband channel matrices from raw measured data. With the help of simulated channel matrices, the signal processing algorithms were tested in noiseless and noisy environments. A multi-measurement channel estimator was presented. With no noise added to the simulation environment, it was shown that this channel estimation contained little or no error. At low SNR, however, the multi-measurement estimator has significant error in its channel estimate. A single measurement channel estimator was presented and shown to perform very well, even in the presence of additive white Gaussian noise. With the use of simulated broadband MIMO data, results from implementations of the single measurement solution are presented to illustrate the minimal error seen in the estimated channel matrices.

Data from an indoor multipath wireless channel was simulated using a ray tracing system. Chapter 4 presented the ray tracing system and the parameters used in the system to simulate the fourth floor of the Clyde Building on the Brigham Young University campus. Permanent structures from the fourth floor were added to the indoor simulations creating a rich multipath environment.

With the data from the ray tracing simulations, the single measurement algorithm was used to estimate the wireless MIMO channels, and analyses were performed on the estimated channel matrix. The analyses of the simulated and modelled channels included a study of the MIMO wideband channel capacity, the coherence bandwidth, and several time domain channel parameters including RMS delay spread, delay interval and maximum delay interval. Through these analyses, the performance of the ray tracing model was compared with that of the SVA model to show very good agreement in channels from the two approaches. The ray tracing model results suggest that the variance for the angles of arrival and the angles of departure might be greater than described by the parameters used for the SVA model. The difference in angular spread is suggested by the slightly higher capacity bounds found for the simulated ray tracing channels.

5.1 Suggestions for Further Research

Although the results presented for this work show the suitability of the SVA model for wideband MIMO communication models, there are still many subsequent areas for further research. The most obvious area for further work, as mentioned earlier, would be to measure wideband data with the MIMO platform that was originally planned to be used in this work. With a measurement platform that is able to properly collect wideband MIMO data, the framework described in this thesis could be applied to estimate the MIMO channels and characterize the channels by computing the wideband MIMO channel parameters. The channel parameters could then be used the same way the ray tracing channel parameters were used in this work to deduce the accuracy of the SVA model for wideband MIMO communication models.

Because the variance of the angle of arrival and the angle of departure seemed somewhat greater for the rays simulated using the ray tracing system than those generated from the SVA model, a further study of the angular variance might be in order. A measurement platform that is capable of detecting angle of arrival and angle of departure could be constructed to more fully analyze the suitability of the SVA model for wideband MIMO communication models.

Once measured data is collected and the wideband MIMO channels are parameterized, these parameters could also be compared with those computed from the electromagnetic ray tracing tool. Because there were only permanent structures constructed in the simulated indoor environment model for the ray tracing system, it would be interesting to see if physical channels could be more accurately simulated with furniture and other non-permanent objects in the simulated indoor environment.

Bibliography

[1] A. Lozano, F. R. Farrokhi, and R. A. Valenzuela, "Lifting the limits on high-speed wireless data access using antenna arrays," *IEEE Communications Magazine*, pp. 156–162, September 2001.

[2] G. J. Foschini and M. J. Gans, "On limits of wireless communications in a fading environment when using multiple antennas," *Wireless Personal Communications*, vol. 6, pp. 311–335, March 1998.

[3] A. A. M. Saleh and R. A. Valenzuela, "A statistical model for indoor multipath propagation," *IEEE Journal on Selected Areas of Communications*, vol. SAC-5, pp. 128–13, February 1987.

[4] Q. H. Spencer, "Modeling the statistical time and angle of arrival characteristics of an indoor multipath channel," Master's thesis, Brigham Young University, 1996.

[5] J. W. Wallace, *Modeling Electromagnetic Wave Propagation in Electrically Large Structures*. PhD thesis, Brigham Young University, 2002.

[6] A. Richter, D. Hampicke, G. Sommerkorn, and R. S. Thoma, "Mimo measurement and joint m-d parameter estimation of mobile radio channels," *IEEE VTS 53rd*, vol. 1, pp. 214–218, Spring 2001.

[7] T. Zwick, D. Hampicke, J. Maurer, and A. Richter, "Results of double-directional channel sounding measurements," *Vehicular Technology Conference Proceedings*, vol. 3, pp. 2497–2501, Spring 2000.

[8] G. Matz, A. F. Molisch, F. Hlawatsch, M. Steinbauer, and I. Gaspard, "On the systematic measurement errors of correlative mobile radio channel sounders," *IEEE Transactions on Communications*, vol. 50, pp. 808 –821, May 2002.

[9] A. Molisch, M. Steinbauer, M. Toeltsch, E. Bonek, and R. S. Thoma;, "Capacity of mimo systems based on measured wireless channels," *Selected Areas in Communications, IEEE Journal on*, vol. 20, pp. 561–569, April 2002.

[10] D. Parsons, *The Mobile Radio Propagation Channel*. Halsted Press: a division of John Wiley and Sons, 1991.

[11] J. W. Wallace and M. A. Jensen, "Statistical characteristics of measured mimo wireless channel data and comparison to conventional models," *IEEE VTS 54th*, vol. 2, pp. 1078–1082, Fall 2001.

[12] T. Svantesson, *Antennas and Progation from a Signal Processing Perspective*. PhD thesis, Chalmers University of Technology, Göteborg, Sweden, 2001.

[13] A. F. Molisch, "A generic model for mimo wireless propagation channels," *IEEE*, pp. 277–281, 2002.

[14] A. Burr, "Evaluation of capacity of indoor wireless mimo channel using ray tracing," *IEEE International Zurich Seminar on Broadband Communications*, February 2002.

[15] B. Lombardi, V. Degli-Esposti, and C. Passerini, "Wideband measurement and simulation of the dect indoor propagation channel," *IEEE Vehicular Technology Conference*, pp. 11–15, 1998.

[16] M. L. Rubio, A. G. Armada, R. P. Torres, and J. L. García, "Channel modeling and characterization at 17 ghz for indoor broadband wlan," *IEEE Journal on Selected Areas in Communications*, vol. 20, pp. 593–601, April 2002.

[17] T. A. Cover and J. A. Thomas, *Elements of Information Theory*. John Wiley and Sons, Inc, 1991.